ChemPhysChem

Chemistry Europe
European Chemical Societies Publishing

Title: Sodiation of hard carbon: how separating enthalpy and entropy contributions can find transitions hidden in the voltage profile

Authors: Michael Mercer, Sam Affleck, Edgardo Maximiliano Gavilan-Arriazu, Alana Aragon Zulke, Philip A. Maughan, Shivam Trivedi, Maximilian Fichtner, Anji Reddy Munnangi, Ezequiel P.M. Leiva, and Harry Ernst Hoster

To be cited as: *ChemPhysChem* 10.1002/cphc.202100748

Link to VoR: https://doi.org/10.1002/cphc.202100748

WILEY-VCH

10.1002/cphc.202100748

Sodiation of hard carbon: how separating enthalpy and entropy contributions can find transitions hidden in the voltage profile

Michael Peter Mercer*[a][b] Sam Affleck[a]
Edgardo Maximiliano Gavilán-Arriazu[c][d]
Alana Aragón Zülke[a][b] Philip A. Maughan[a]
Shivam Trivedi[e] Maximilian Fichtner[e]
Anji Reddy Munnangi[f] Ezequiel P.M. Leiva[c]
Harry Ernst Hoster[a][b][g]

Abstract

Sodium-ion batteries (NIBs) utilise cheaper materials than lithium-ion batteries (LIBs), and can thus be used in larger scale applications. The preferred anode material is hard carbon, because sodium cannot be inserted into graphite. We apply experimental entropy profiling (EP), where the cell temperature is changed under open circuit conditions. EP has been used to characterise LIBs; here, we demonstrate the first application of EP to any NIB material. The voltage versus sodiation fraction curves (voltage profiles) of hard carbon lack clear features, consisting only of a slope and a plateau, making it difficult to clarify the structural features of hard carbon that could optimise cell performance. We find additional features through EP that are masked in the voltage profiles.

---

*Corresponding author e-mail: m.mercer1@lancaster.ac.uk

[a] *Dr. M.P. Mercer, Mr. S. Affleck, Dr. P.A. Maughan, Dr. A.A. Zülke and Prof. H.E. Hoster, Department of Chemistry, Lancaster University, Bailrigg, Lancaster, LA1 4YB, UK*

[b] *Dr. M.P. Mercer, Dr. A.A. Zülke and Prof. H.E. Hoster, The Faraday Institution, Quad One, Harwell Science and Innovation Campus, Didcot, UK*

[c] *Dr. E.M. Gavilán-Arriazu and Prof. E.P.M. Leiva, Departamento de Química Teórica y Computacional, Facultad de Ciencias Químicas, Universidad Nacional de Córdoba, INFIQC, Córdoba, Argentina*

[d] *Dr. E.M. Gavilán-Arriazu, Facultad de Matemática, Astronomía y Física, IFEG-CONICET, Universidad Nacional de Córdoba, Córdoba, Argentina*

[e] *Mr. S. Trivedi and Prof. M. Fichtner, Helmholtz Institute Ulm (HIU), D-89091, Ulm, Germany*

[f] *Dr. A. Reddy Munnangi, Faculty of Science and Engineering, Swansea University, Fabian Way, Swansea, UK*

[g] *Prof. H.E. Hoster, Department of Mechanical and Process Engineering, University Duisburg-Essen, Lotharstraße 1, 47057 Duisburg, Germany*

We fit lattice gas models of hard carbon sodiation to experimental EP and system enthalpy, obtaining: 1. a theoretical maximum capacity, 2. interlayer versus pore filled sodium with state of charge.

Keywords

thermodynamics, batteries, hard carbon, sodium-ion, entropy

1 Introduction

The demand for clean and sustainable energy sources necessitates effective and low cost energy storage solutions. Lithium-ion batteries (LIBs) have been highly prolific in portable devices and in mobile transport applications. The cost of the raw materials of LIBs, and the fact that lithium is limited in supply and unevenly distributed throughout the globe raises challenges for large scale applications of LIBs in areas like stationary storage [1, 2, 3]. Sodium-ion batteries (NIBs) are an attractive alternative, replacing lithium with much more Earth-abundant sodium. NIBs share many similarities with LIBs, comprising an organic electrolyte and, typically, a layered transition metal oxide as cathode material [4, 5]. A key challenge has been the development of suitable anode materials. The usual anode material of choice for LIBs, graphite, does not intercalate sodium to any significant extent [6].

As an anode material for NIBs, hard carbon has attracted much interest since reports of sodium insertion into its structure by Stevens and Dahn [7, 8]. Hard carbons consist of randomly oriented, curved and defective layers of graphene separated by large interplanar distances [9]. In a simplified picture, the structure can be understood by a “house of cards” model [7]. Sodium can be inserted at defect sites, between the carbon layers, and into nanopores [9, 10, 7, 8, 11, 12, 13, 14]. Galvanostatic charge/discharge profiles comprise two main features: **1**: a sloping region from the maximum voltage of 2 V (vs. Na) to approximately 0.1 V; **2**: a plateau below 0.1 V [15]. Stevens and Dahn used small and wide angle X-ray scattering (SAXS/WAXS) to assign sodium intercalation to the sloping voltage region, and filling of the nanopores to the low voltage plateau [8]. Nuclear magnetic resonance (NMR) suggested a similar interpretation [9, 10]. However, a key challenge in this area is that the voltage profile itself does not contain any distinct features apart form the slope and plateau. The processes giving rise to these features may be interdependent and overlap, but there isn’t enough information to separate them. In this regard, local probes and *operando* techniques like SAXS, WAXS, Raman and NMR have provided physical insight, but further work is needed to quantify, in particular, the proportions of sites occupying the interlayers and the nanopores at a given cell voltage.

A virtually unexplored parameter in NIB characterisation is the effect of temperature variation. As well as influencing the kinetics of the various sodium insertion processes, the voltage profile is directly connected to temperature by the partial molar entropy of sodium insertion [16]. To measure this parameter, it is necessary to probe the open circuit voltage (OCV) of the cell by performing a technique similar to galvanostatic intermittent titration technique (GITT), i.e. interrupted galvanostatic pulses and measurement of the cell voltage at rest [17, 18, 19]. In so called "entropy profiling", the cell OCV of the cell is measured while changing the cell temperature (c.f. section 2.3 for further details). The only additional requirements compared with standard electrochemical characterisation are a temperature controller and high-resolution voltage measurement. This technique has been extensively applied in the LIB area [20, 21, 22, 23, 24, 25, 26, 27, 28, 29, 30] but surprisingly, has not yet been applied to any NIB chemistry. In previous work, we combined experimental entropy profiling with lattice gas models and in so doing, gained additional interpretation of ordering phenomena in lithium manganese oxide spinel [20, 21] and lithium insertion/deinsertion in graphite [22, 23].

In the present work, we transfer established entropy profiling methodology to sodiation in hard carbon. In section 2, we outline the experimental methods and protocols, including a summary of how all the thermodynamic variables are obtained from the experimental results, which follow in section 3. Detailed interpretation of those results depends on models to separate interlayer and nanopore filling. Two approaches, the Bragg-Williams model and grand canonical Monte Carlo, are outlined in section 4. We show, by fitting interaction parameters within these models to experimental data (section 5) how additional interpretation of the energetics of sodium insertion in the interlayers and nanopores can be obtained that would be impossible to achieve from OCV measurement alone. Overall, the work demonstrates how the additional features revealed by entropy profiling in combination with models can be applied to gain insight into sodium insertion processes, with the potential to transfer this methodology to a wider range of synthesised hard carbon materials.

2 Experimental Methods

2.1 Coin cell assembly and materials

Electrochemical studies were carried out using stainless steel CR2032 2-electrode coin cells. Working electrode materials were prepared by mixing hard carbon powder, prepared according to a previous publication [12], with polyvinylidene fluoride (PVDF) binder in a mass ratio of 90:10. N-methyl-2-pyrrolidinone (NMP) was used as the solvent to prepare a slurry, which was cast onto aluminium foil as the current collector. The electrodes were dried at 80°C overnight, before transferring to an argon-filled glovebox (H_2O and O_2 levels < 0.1 ppm) for cell construction. 16 mm disks were punched, giving a typical hard carbon mass loading of around 2-2.5 mg cm^{-2} per cell.

Sodium metal (Tob New Energy) disks were used as the counter and reference electrode. All voltages are, consequently, reported with respect to metallic sodium. Whatman micro glass fibre paper was used as the separator and the electrolyte was 1 M $NaClO_4$ (anhydrous, $>$ 98% purity, Alfa Aesar) in a solution mixture of propylene carbonate (PC, anhydrous, 99.7% purity, Sigma Aldrich) /Fluoroethylene carbonate (FEC, anhydrous, $>$ 99% purity, Sigma Aldrich) in a 98:2 mass ratio. The PC and FEC were dried in the glovebox using molecular sieves for 48 h before electrolyte preparation.

2.2 Electrochemical measurements

Experimental measurements were performed using aluminium heat exchangers, in direct thermal contact with the coin cells, which were connected to a Julabo F12 refrigerated – heating circulator, allowing direct control over the cell temperatures. This setup enabled more rapid thermal equilibration of the cells than would be possible using a climate chamber. The temperature was monitored by type-T thermocouples in direct contact with the heat exchangers. A Keysight 34970A data acquisition system with multiplexer unit was used for high resolution (22 bit) voltage and temperature measurements, assisting post processing of entropy profile data. Cell current and voltage were controlled by a BaSyTec CTS cycler. A software interface between the data acquisition unit and the battery cycler allowed real time measurement of temperature, current and voltage to the required resolution. Data points were recorded every 1 s. Further detail of the setup, applied to Li-ion half cells and commercial cells, can be found in earlier publications [24, 23, 21, 22].

Freshly assembled cells were subjected to the following protocol, at controlled $T = 25°C$: 5 cycles between 1.5 to 0.05 V at 10 mA/g (here, the mass is the amount of hard carbon active material). 3 further cycles were performed subsequently between 2.0 and 0.005 V at 10 mA/g and revealed cell capacities in agreement with previous characterisation on the same hard carbon material at the same cycle rate and potential limits [12]. Rest periods of 20 minutes were inserted between each charge and discharge cycle. This procedure was performed to check representative and stable cycling behaviour before entropy profiling characterisation.

2.3 Entropy profiling

All measurements described subsequently were preceded by a constant current/constant voltage (CCCV) charging protocol to ensure a consistent starting sodiation state for each experiment. This stage consisted of galvanostatic charge at 10 mA/g up to 2.0 V, followed by at least 2 hours of polarisation at 2.0 V. This ensured a consistent starting state for the entropy profile measurements, with the hard carbon structure commencing as close to fully desodiated as possible, in line with protocols that we have previously applied to Li-ion cells [24, 23, 21, 22].

We used similar methods as in our previous work [24, 23, 21, 22] to obtain entropy profiles for hard carbon. The method is akin to galvanostatic intermittent titration technique (GITT), comprising alternating steps under galvanostatic control followed by relaxation under open circuit conditions [17, 18], but in addition the temperature is varied during the relaxation period and entropy is calculated from the gradient of OCV with temperature. Measurements comprised iterative steps of galvanostatic discharge at 10 mA/g followed by a total of 80 minutes of relaxation time. The current and temperature were changed dynamically, as outlined in Table 1. Each iteration was repeated until the cell voltage was less than 0.005 V.

Table 1: Conditions applied during each iteration of the entropy profiling experiments.

Step	Time (min)	Temperature T (°C)
Discharge (10 mA/g)	20	20
OC at T_1	20	20
OC at T_2	20	15
OC at T_3	20	10
OC at T_1	20	20

2.4 Determination of thermodynamic variables

It is well known [22] that the equilibrium cell voltage, $\phi(x)$ and chemical potential of the guest atom (Na in this case), $\mu(x)$ are related as

$$\phi(x) = -\frac{\mu(x) - \mu_{\mathrm{Na}}^{\mathrm{ref}}}{nF}, \tag{1}$$

where $\mu_{\mathrm{Na}}^{\mathrm{ref}}$ is the chemical potential of the metallic Na anode reference, which is defined as zero on our reference scale. $n = 1$ is the number of electrons transferred per inserted Na atom, and F is the Faraday constant. With a suitable choice of units for all potentials (μ expressed in eV per inserted atom), this can be written much more simply as

$$\phi(x) = -\mu(x). \tag{2}$$

The term $\mu(x)$ can also be written as

$$\mu(x) = \left(\frac{\partial G(x)}{\partial x}\right)_{p,T,N_{\mathrm{host}}}, \tag{3}$$

where p = pressure, T = the absolute temperature, N_{host} and N_{Na} are respectively the number of carbon and sodium atoms in the system. G is the Gibbs free energy per inserted Na atom. The subscripts p, T and N_{host} will be implicitly assumed constant from now on and dropped for simplicity.

Here, we define x ($0 \leq x \leq 1$) as the fraction of sodium in the host. It is straightforward to define $x = 0$ as the point where the experimental discharge capacity, Q, is zero, because we initialise the experiment from a CCCV condition, and thus the hard carbon ostensibly starts fully desodiated. It is necessary to define a theoretical maximum capacity to determine $x = 1$. The maximum experimental discharge capacity, $Q_{\max}^{\mathrm{expt}}$ is attained when the 0 V cutoff criterion is reached, but additional sites could in principle be available to be filled with sodium below 0 V. Fortunately, the Bragg-Williams model defined later in section 4.1 allows a theoretical maximum capacity, $Q_{\max}$, to be determined through fitting the thermodynamic variables to the experimental data. We can then define x as

$$x = \frac{Q}{Q_{\max}}, \tag{4}$$

where Q is the measured capacity obtained from experiment in mAh/g. We can similarly define

$$x_{\mathrm{expt}} = \frac{Q}{Q_{\max}^{\mathrm{expt}}}, \tag{5}$$

where x_{expt} similarly goes from 0 to 1. However, with $Q_{\max} > Q_{\max}^{\mathrm{expt}}$, there is a conversion factor required to relate simulated and experimental data on an equivalent Q scale, which is detailed further in the Supplementary Information, section 3.2.

The partial molar Gibbs free energy, ΔG, can be written as

$$\frac{\partial G(x)}{\partial x} = \frac{\partial H(x)}{\partial x} - T\frac{\partial S(x)}{\partial x} = \Delta G, \tag{6}$$

where $H(x)$ and $S(x)$ are the enthalpy and entropy, respectively, per formula unit of host material.

Assuming that the OCV, E_{OCV}, measured at the end of the relaxation period for each x value corresponds to $\phi(x)$, we can use equations 2, 3 and 6 to get $\partial G/\partial x = -E_{\mathrm{OCV}}$. Hence we obtain

$$\frac{\partial S(x)}{\partial x} = \frac{\partial E_{\mathrm{OCV}}(x)}{\partial T} = \Delta S \tag{7}$$

and

$$\frac{\partial H(x)}{\partial x} = T\frac{\partial E_{\mathrm{OCV}}(x)}{\partial T} - E_{\mathrm{OCV}}(x) = \Delta H. \tag{8}$$

Due to the choice of units of eV per formula unit for the potentials $H(x)$ and $TS(x)$, i.e. as in the conversion between equations 1 and 2, the usual factors of F have been omitted. In this way, we can relate the partial molar entropy and enthalpy, ΔS and ΔH respectively, in units of eV per inserted Na atom. All of the terms in equations 7 and 8 are measurable using methods described in section 2.3.

3 Experimental results

Galvanostatic characterisation of hard carbon cells, using procedures described in section 2.2, is shown in Figure 1. Cycle 1, indicated in the inset shows a large irreversible loss of capacity of about 70 mAh/g, corresponding to the formation of a stable solid electrolyte interphase (SEI). Cycles 2-5 show stable

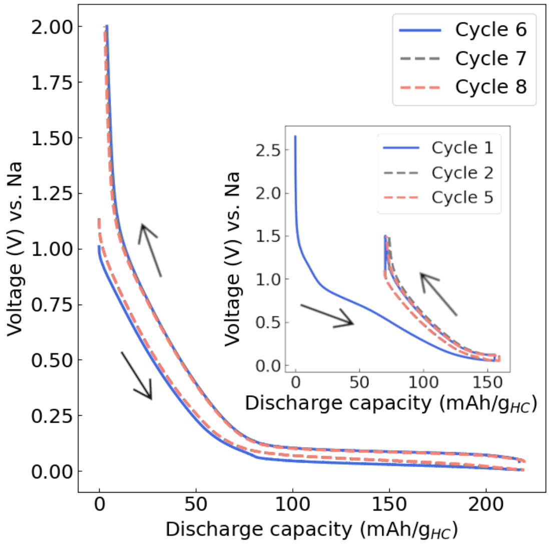

Figure 1: Galvanostatic cycles at 10 mA/g. Cycles 1-5 cycles were performed between 1.5 to 0.05 V. The subsequent 3 cycles, between 2.0 and 0.005 V, are denoted cycles 6-8. Arrows indicate the cycling direction.

cycling behaviour. The discharge capacity obtained during cycles 6-8 corresponds to approximately 220-230 mAh/g, in good agreement with previously published work performed in the same potential window with the same hard carbon material [12] and these scans show a stable and repeatable behaviour. This behaviour displays the characteristic sloping region up to approximately 80 mAh/g, followed by a plateau between 80 mAh/g and maximum capacity. The voltage difference between sodiation and desodiation (hysteresis) has been widely reported elsewhere [12, 7, 8, 19], but all subsequent discussion relates to the sodiation behaviour.

The open circuit voltage (OCV) behaviour, as well as the entropy and enthalpy profiles are shown in Figure 2. These results were obtained using the procedure described in section 2.3, after attaining the stable cycling behaviour shown in Figure 1. The partial molar (p.m.) entropy and enthalpy, ΔS and ΔH, were obtained with equations 7 and 8, respectively. Note the scales on the y-axes - these are presented such that addition of -ΔH (Figure 2a) to $T\Delta S$ (Figure 2b) gives -ΔG, and thus by equations 2- 6 the OCV shown in Figure 2c, without any further unit conversion being necessary.

Firstly, the OCV shown in Figure 2c, effectively obtained under GITT conditions, displays the same features and voltage scale as the result obtained under continuous galvanostatic discharge (sodiation). This is expected as each entropy profiling step was initialised by a discharge step for 20 minutes, and indicates that both measurements probe stable or at least metastable behaviour (that is, the galvanostatic data can be considered as a pseudo OCV measurement).

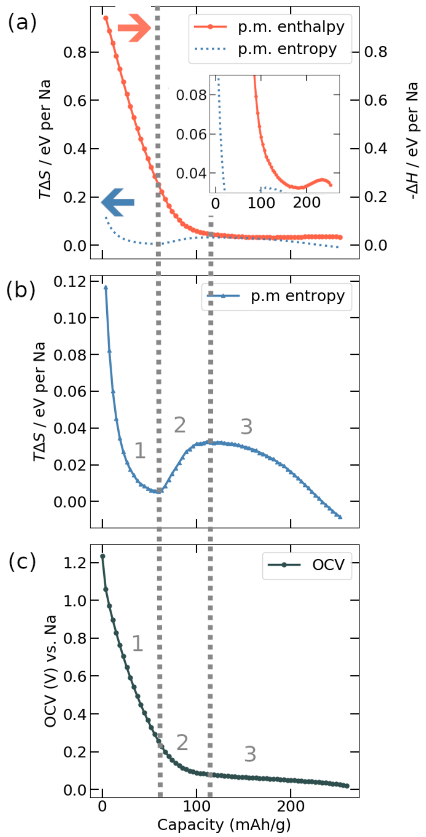

Figure 2: (a) Partial molar (p.m.) enthalpy, (b) p.m. entropy and (c) open circuit voltage (OCV) obtained for the hard carbon material. In (a), the p.m. entropy is also shown on the same energy scale; arrows indicate the relevant axes. The inset in (a) shows the same data over a narrower energy scale. The regions of the plots demarked **1-3** are described in the main text; the boundaries between these regions are determined by the turning points in (b).

Although the mechanisms are still disputed, the sloping region, which here terminates at approximately 70-80 mAh/g, is generally associated with the insertion of sodium into the carbon layers. The layer filling is hypothesised to initiate at defect sites and then proceed in the layers up to a stoichiometry of approximately NaC_{24} [12]. The voltage plateau above 70-80 mAh/g capacity is primarily attributed to insertion of sodium in the nanopores, with interlayer sodium insertion thought not to contribute significantly here.

The three regions in Figure 2 marked **1-3** correspond approximately to: **1**: sloping region; **2**: transition; **3**: plateau region. Comparing the three panels of Figure 2, it is apparent that the sloping region **1** (capacity < 80 mAh/g) of the OCV curve is dominated by the p.m. enthalpy (Figure 2a), which spans an energy scale of approximately 0 to 1 eV. The p.m. enthalpy changes in slope between approximately 80-110 mAh/g (region **2**) and in the plateau region **3**, the p.m. enthalpy is almost completely flat while the OCV still displays a slope in this region. However, the inset of Figure 2a reveals a local minimum in $-\Delta H$ of approximately 0.03 eV at capacity $\approx$190 mAh/g, and a local maximum at capacity $\approx$230 mAh/g, the significance of which will be explored further in section 5.3.

The p.m. entropy shown in Figure 2b displays several distinct features. Between about 0 to 80 mAh/g capacity, the p.m. entropy decreases monotonically with increasing in capacity (interval **1**). Between approximately 70 to 110 mAh/g, there is an increase in p.m. entropy (interval **2**). After a local maximum in p.m. entropy, there is again a decrease from about 110 mAh/g to the capacity maximum of 272 mAh/g (interval **3**). The p.m. entropy plays an important role in the plateau region. The decrease in the p.m. entropy between 120 and 272 mAh/g is the primary contribution to decrease in the OCV (Figure 2c) in the plateau region.

The observed decrease, increase and decrease in p.m. entropy in intervals **1-3** shown in Figure 2b is reminiscent of similar behaviour observed in the entropy profiles of Li-ion systems. It has been observed and explained in lithium manganese oxide (LMO) spinel [20, 21], layered lithium cobalt oxide (LCO) [25] and graphite [26, 23, 22]. In these systems, the maximum and minimum p.m. entropy within **2** is associated with ordering of lithium in the lattice, while the rapid change in p.m. entropy such as in intervals **1** and **3** is indicative of a transition to disordered ideal solid solution behaviour at low and high lithium occupation in the lattice, respectively. Quantitative interpretation of the observed features in the context of the present sodium-ion system requires a model, which is presented and discussed in section 4. In this model, the entropy features naturally arise as sodium transitions from interlayer to nanopore filling.

Additionally, numerical differentiation of the OCV with respect to x (as defined in section 2.4) was performed using the "gradient" function in the NumPy module of Python 3, which uses second order central differences in the interior points. Using the variables defined in section 2.4 and applying the chain rule, it is found that (c.f. Supplementary Information, section 3.2 for further details)

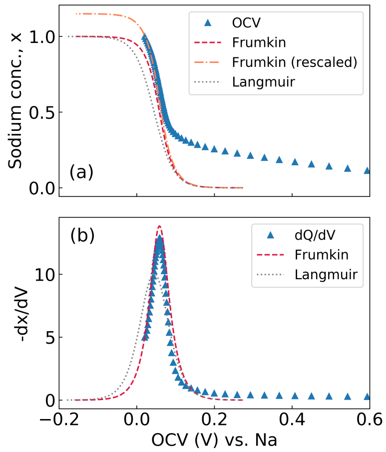

Figure 3: (a) Experimental OCV data; (b) dQ/dV results obtained from equation 9. These results are compared with a Frumkin isotherm with interaction parameter, $g = -25$ meV (red dashed line) and $g = 0$ meV (grey dotted line; equivalent to a Langmuir isotherm).

$$\frac{dQ}{dV} = -\frac{dx_{\text{expt}}}{dE_{\text{OCV}}(x)} = -\frac{1}{k^2}\left(\frac{dx}{dE_{\text{OCV}}(x)}\right), \tag{9}$$

where $k = Q^{\text{expt}}_{\text{max}}/Q_{\text{max}}$, and the minus sign emerges because the measurement was performed by galvanostatic discharge. Thus, dQ/dV was obtained as shown in Figure 3b.

The single peak observed corresponds to the voltage plateau in Figure 3a. The sloping region in the OCV does not display any inflection points or additional plateaus and therefore does not result in a dQ/dV peak.

The single dQ/dV peak in Figure 3b can be approximately described with a Frumkin isotherm [31], where the cell voltage $E(x)$ is given by

$$E(x) = \epsilon_0 - k_B T(x\log(x) + (1-x)\log(1-x)) + gx, \tag{10}$$

where ϵ_0 is an interaction term between Na and the host that shifts the voltage scale, k_B is the Boltzmann constant, T is the temperature, and g is an interaction term between Na-Na pairs. The experimental peak full width half maximum (FWHM) value is found to be less than 90 mV. Within this framework, this FWHM value corresponds to attractive interactions ($g < 0$) between the inserted sodium atoms in the plateau region, as shown by the red dashed line. A FWHM $>$ 90 mV would indicate repulsion, while a FWHM $=$ 90 mV would be equivalent to the Langmuir isotherm with $g = 0$ (grey dotted line in Figure 3a-b).

The fit with the Frumkin isotherm reveals several deficiencies that are all addressed by the model presented in the next section:

1. The sloping voltage region is not properly described.
2. The configurational entropy term in equation 10 is that of an ideal solid solution, at variance with the result shown in Figure 2b.
3. An attractive pairwise term would cause ΔH to decrease linearly with increasing inserted sodium fraction (i.e. capacity) in the plateau region, but as remarked above, ΔH shows two turning points in the inset of Figure 2a. This suggests additional, possibly higher order interactions in the system.
4. There is a discrepancy between the voltage profile obtained with high x. This could indicate that there is, in principle, additional sodiation capacity beyond $x = 1$. To illustrate this point, the Frumkin isotherm fit is extrapolated beyond $x = 1$ (dash-dot line in Figure 3a).

Hence, further interpretation of the experimental thermodynamic data for sodium insertion in hard carbon requires a model that can quantitatively separate the contibutions from defect insertion, carbon interlayer filling and insertion of sodium into the nanopores. This framework is presented in the following section.

4 Simulation methods

4.1 Mean field modelling

We apply a two-level Bragg-Williams approach to model the thermodynamics of sodium insertion in hard carbon. In the model, the system is represented in two energy levels, where level 1 represents insertion of sodium into the carbon interlayers while level 2 represents occupation of sodium in the pores. We denote these environments as sublattices 1 and 2, where N_1 and N_2, respectively, represent the total number of atoms currently occupying each level, and $N = N_1 + N_2$, where N represents the total number of occupied sites in both levels. A schematic representation of the model is shown in Figure 4. We solve this model in the canonical ensemble, i.e. by varying the number of particles in the system. This method has been applied, in similar form, by some of us to understand voltage profiles, and entropy/enthalpy transitions in lithium manganese oxide [21] and lithium (de)insertion in graphite [23, 22, 32]. Some model parameters were fitted to experimental data in a multiple stage numerical optimisation procedure that is further detailed the Supplementary Information, section 3.1. For convenience, we summarise here all the input parameters in Table 2, and further details of the interpretation are described in the text.

We represent the total number of available sites in the interlayers and nanopores, with M_1 and M_2, respectively, where here $M_1 \neq M_2$[23, 22, 32], since it is not

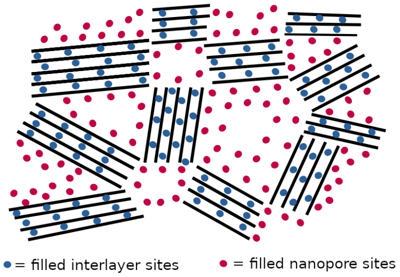

Figure 4: Representation of the site placements in the hard carbon model. Black lines denote graphene layers. Blue sites correspond to interlayer sublattice, n_1, red sites correspond to filling of nanopores in sublattice n_2. Here all the sites are completely filled (sodiation fraction $x = 1$).

known *a priori* what the maximum number of sites is in the interlayers or nanopores. The sublattice occupancies, n_1 and n_2, are defined as $n_1 = N_1/M_1$ and $n_2 = N_2/M_2$. The ratio L ($0 < L < 1$), determined through fitting, is given by $L = M_1/(M_1 + M_2)$. The convergence of the thermodynamic results with respect to system size was checked and it was found that a total of $M_1 + M_2 = 400$ sites was more than sufficient for all values of L. The system size convergence was checked during the optimization procedure as detailed further in the Supplementary Information, section 3.2.

We define the sodiation fraction, x ($0 \leq x \leq 1$), as

$$x = Ln_1 + (1 - L)n_2, \tag{11}$$

so that $0 \leq n_1 \leq 1$ and likewise for n_2. For the more complex interactions in the hard carbon system that will be described shortly, the partition function must be solved numerically, and then all thermodynamic properties can be obtained from analytical expressions.

The partition function, $Q(N, M_1, M_2)$, is [32]

$$Q(N, M_1, M_2) = \sum_i e^{-\frac{E_i}{k_B T}} = \sum_{j=0}^{N} \Omega_j e^{-\frac{E_j}{k_B T}}, \tag{12}$$

where the index i indicates summation over all possible Na/vacancy configurations while index j indicates summation over degenerate (energetically equivalent combinations of) levels, E_j, where the degeneracy, Ω_j, is defined in the Supplementary Information, section 1, and k_B is the Boltzmann constant.

The assumption of the Bragg-Williams approximation is that all Na/vacancy configurations for a particular set of values n_1 and n_2 are degenerate, where the number of degenerate energy levels is Ω_j for each state j [32]. The calculation is performed by enumerating through all possible values of n_1 and n_2 for a given x value, where n_1 and n_2 are determined by the index j. The mean field

Table 2: Summary of input parameters in the mean field model. Values reported in the top part of the table were fixed where indicated; fitted parameter values reported at the right of the table were the ones obtained at the end of the numerical optimisation procedure (c.f. Supplementary Information, section 3.1 for further details). For values that are allowed to vary, the range of allowed values is reported in the right column.

Parameter	Definition	Value
N	Total number of filled sites	$0 \leq N \leq M_1 + M_2$
M_1	Number of available interlayer sites	
M_2	Number of available nanopore sites	
M_{tot}	Total number of available sites	$M_{\text{tot}} = M_1 + M_2 = 400$
x	Overall sodium concentration $x = N/(M_1 + M_2)$	$0 \leq x \leq 1$
n_1	Interlayer sublattice concentration	$0 \leq n_1 \leq 1$
n_2	Nanopore sublattice concentration	$0 \leq n_2 \leq 1$
T	Absolute temperature	288 K
	Fitted parameters	
L	Ratio of interlayer/total sites	0.329
$\epsilon_1'(n_1)$	Interlayer point interaction term between sodium and carbon $\epsilon_1'(n_1) = \epsilon_1 + A\exp(-\mathrm{Bn}_1^{\mathrm{C}})$	Varies with n_1
ϵ_1	Interlayer point term at high sodium occupation	-0.372 eV
A	Function amplitude	-0.684 eV
B	Function decay constant	1.874
C	Function exponent	1.686
ϵ_2'	All interaction terms in nanopores $\epsilon_2'(n_2) = \epsilon_2 + g_2 n_2 + g_3 n_2^2$	Varies with n_2
ϵ_2	Nanopore point term interaction	-0.021 eV
$\Delta\epsilon$	$\Delta\epsilon = \epsilon_1 - \epsilon_2$ (point term difference)	-0.351 eV
g_2	Mean field interaction between Na-Na pairs in the nanopores	-0.046 eV
g_3	Mean field interaction between Na triplets in the nanopores	0.032 eV
$Q_{\max}$	Theoretical maximum capacity obtained when $x = 1$	338 mAh/g
ΔS_{corr}	Partial molar entropy correction (non-configurational entropy)	4.50 J mol^{-1} K^{-1}

approximation means that the energy expression is not affected by the local arrangement of Na atoms, only the proportions occupying the two levels.

We can write the interaction Hamiltonian, $H(N, M_1, M_2)$ as

$$H(N, M_1, M_2) = \epsilon'_1 N_1 + \epsilon'_2 N_2, \tag{13}$$

where $N_1 = n_1 M_1$ and $N_2 = n_2 M_2$ are the total number of atoms on sublattices 1 and 2 respectively. The terms ϵ'_1 and ϵ'_2 refer to the interaction terms in the interlayer and pore sublattices, respectively. The definition, physical justification and interpretation behind the ϵ'_1 term in the interlayers is presented in section 5.1.

We assume a point term, ϵ_2, that is constant in the pores because the interactions there are predominantly metallic in nature [10, 9]. On the basis of the cited NMR studies, complete reduction of Na^+ to Na^0 should occur, indicative of complete charge transfer. Therefore, in contrast with the interlayer interactions, we do not expect significant variations in electronic state with nanopore sodiation fraction, and therefore the Na-C interaction is expected to be constant with respect to the sodium coverage. However, the dQ/dV data in Figure 3b additionally suggests interparticle interactions between sodium atoms in the pores. Thus the overall nanopore interaction term, ϵ'_2, can be represented as

$$\epsilon'_2 = \epsilon_2 + g_2 n_2 + g_3 n_2^2, \tag{14}$$

where g_2 represents an interaction between Na-Na pairs in the pores (analagous to the Frumkin parameter g introduced in section 3) and g_3 is a triplet interaction parameter. This was found to be the minimum complexity needed to replicate the peak FWHM while avoiding overfitting. Further detail and physical justification for nanopore interaction term ϵ'_2 is detailed in section 5.3.

As for the energy terms, E_j, in equation 12, these can be determined for each index j, as

$$E_j = \begin{cases} (N-j)\epsilon'_1 + j\epsilon'_2 = N_1\epsilon'_1 + N_2\epsilon'_2 & \text{for } N < M_{\mathrm{tot}}/2 \\ (M_1 - j)\epsilon'_1 + (N - M_2 + j)\epsilon'_2 = N'_1\epsilon'_1 + N'_2\epsilon_2 & \text{otherwise,} \end{cases} \tag{15}$$

where $N'_1 = M_1 - N_1$ and $N'_2 = M_2 - N_2$, i.e. N'_1 and N'_2 denote the number of vacant sites in sublattices 1 and 2, respectively. The index j in the top (bottom) line of equation 15 denotes the number of filled (vacant) sites in sublattice 2, respectively. Counting through all values of j in equation 12 allow the energy of all possible combinations of N_1 and N_2 to be determined for a given N. The second line of equation 15 is simply a numerical trick to reduce the number of states to count in the summation.

Once the equation 12 is determined, all of the thermodynamic relationships can easily be obtained. For example, the chemical potential of inserted Na, μ, can be determined as

$$\mu = -k_B T \left(\frac{\partial \ln Q}{\partial N} \right)_{T, M_1, M_2}, \tag{16}$$

and hence the open circuit voltage versus metallic Na is given by $E_{\mathrm{OCV}} = -\mu$. All other thermodynamic variables can be then obtained from equations 3-8, including the enthalpy $H(x)$ and configurational entropy $S_{\mathrm{conf}}(x)$.

The partition function calculated above naturally includes all configurational degrees of freedom, but in principle there are also vibrational and electronic contributions to the entropy. Based on assumptions of Fultz et al., we treat the vibrational and electronic contributions as constant, given that in lithium ion systems, they do not vary substantially with lithiation degree [25, 26]. Likewise, there is no evidence to suggest these contributions vary significantly with sodiation degree, x, here. The correction to the partial molar entropy, ΔS_{corr} is therefore

$$\Delta S(x) = \frac{\partial S(x)}{\partial x} = \frac{\partial S_{\mathrm{conf}}(x)}{\partial x} + \Delta S_{\mathrm{corr}}, \tag{17}$$

where ΔS_{conf} is the partial molar configurational entropy determined by solving the partition function, ΔS_{corr} is a constant fitted parameter and $\Delta S(x)$ includes all entropy contributions.

Good agreement between experimental and simulated data was obtained by applying the numerical optimisation procedure, described in Supplementary Information, section 3.1, with the Hamiltonian defined in equation 13.

4.2 Grand canonical Monte Carlo calculations

Grand canonical Monte Carlo (GCMC) calculations were performed with two different types of site, c_i and c_j, which refer to the interlayer and nanopore site occupancies, respectively. c_i takes value 0 if an interlayer site is empty and 1 if the site is filled, and likewise for c_j. A total of $M_1 + M_2 = 5000$ sites was found to be fully converged with respect to the system size, as further detailed in the Supplementary Information, section 4. GCMC calculations were perfomed using the Metropolis algorithm [33], with a total of 5000 Monte Carlo steps (MCS) per site run at each input chemical potential μ to reach equilibrium. A further 5000 MCS per site were run subsequently, and fluctuations of the occupancy, N and internal energy U at each μ value were sampled every 200 Monte Carlo steps and were used to derive thermodynamic observables, as further detailed in our previous work [20, 34].

A grand canonical Hamiltonian of the form

$$H = (\epsilon_1' - \mu) \sum_{i}^{M_1} c_i + (\epsilon_2' - \mu) \sum_{j}^{M_2} c_j, \tag{18}$$

was used in all GCMC calculations, where the terms were defined in section 4.1. Different variations of the ϵ_1' are presented in the following section, while nanopore interaction term ϵ_2' is as defined in equation 14. Otherwise, the same nomeclature and parameter values were used as described in section 4.1.

We used GCMC simulations to test the effect of different point term distributions in the interlayers, which is not feasible with the partition function defined in equation 12. Additionally, this method allowed us to verify the simulation results obtained with the Bragg-Williams method, using the same interaction parameters, to verify the calculation of the partition function.

5 Comparing lattice gas models to experiments

5.1 Interpretation of sloping voltage region

The layers of hard carbon are highly heterogenous, comprising a variety of possible point defects [10, 8, 12, 11]. Point terms for sodium adsorption in carbon nanostructures have been computed elsewhere by DFT, including sodium adsorption near possible defects such as oxygenated sites and carbon vacancies [11, 12]. In the cited studies, these point terms were found to span an energy range of approximately 0 to -1 eV versus Na metal. We assessed the influence of different interlayer site distributions by performing GCMC calculations, detailed in section 4.2.

An analysis of different distributions, and the dependence of simulation results with system size, is presented in the Supplementary Information, section 4. In Figure 5, a triangular distribution of interlayer site energies, ϵ_1', is presented. In the GCMC model, energies of the interlayer sites were chosen by running through each of the sites and assigning them an energy using a random sample of the frequency distribution. This distribution naturally includes a low proportion of sites with high binding energy, with a linearly increasing fraction of sites with lower binding energy, with the frequency distribution of ϵ_1' shown in Figure 5a. The upper and lower limits of the distribution, 0.08 eV and -1.65 eV respectively, were obtained by comparing the Monte Carlo results with the experimental enthalpy profile. The physical picture is also shown schematically in Figure 5b.

GCMC simulation results obtained with ϵ_1' following a triangular distribution are presented in Figure 6. Here, the experimental x scale was obtained by normalising the discharge capacity to the theoretical maximum capacity $Q_{\mathrm{max}} =$ 338 mAh/g. This capacity value is comparable with experimental maximum capacities obtained from other hard carbons [35], with a value as high as ≈430 mAh/g having been reported [36]. The grey and green lines represent extreme cases: the grey line is the entropy of an ideal solid solution, where all lattice sites are filled randomly, which is described by equations S7-S8. The green line corresponds to random filling of interlayer sites until all sites are filled, followed by random filling of nanopore sites. The green line is described by equations S12-S15.

Most of the features of the sloping region of the experimental OCV (Figure 6a), are well replicated by the GCMC simulations. Some deviation in the p.m. enthalpy (Figure 6b) is observed at the transition at $x = 0.3$. This is reflected also in the p.m. entropy, Figure 6c, at the same x value, which shows a more pronounced step than observed in experiment. Another difference between experiment and the model is that the p.m. entropy from GCMC remains almost

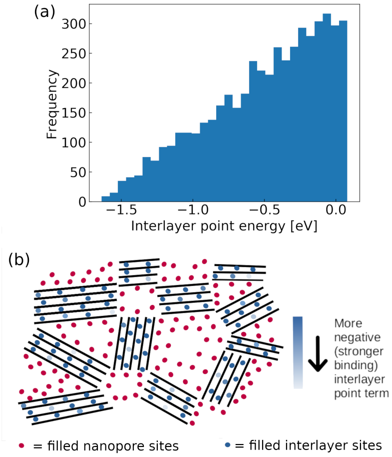

Figure 5: (a) Triangular distribution of site energies in interlayer sublattice n_1. Site energies were binned in intervals of 0.1 eV to obtain the frequency. (b) Schematic representation of the inclusion of interlayer point defects. The lattice is shown to be completely filled ($x = 1$). There is a small proportion of lighter blue sites (energy close to -1.65 eV). The majority of interlayer sites are dark blue, indicating less negative binding energy closer to 0.08 eV. Red sites indicate occupation of sodium in the pores, which are treated as having the same energy.

constant between $0 < x < 0.3$, while the experimental result is much closer to the red dashed line.

The experimental configurational entropy, shown in Figure 6d, was obtained from equation S16. The procedure is detailed in full in the Supplementary Information, section 2.2, and a very similar approach has previously been used to determine the experimental configurational entropy for lithium insertion/removal in graphite [22].

In Figure 6d, it is apparent that the simulated point term heterogeneity leads to almost zero S_{conf} between $0 < x < 0.3$, contrary to the experimental S_{conf}, which agrees much more closely with interlayer solid solution filling (red dashed line). The reason for the very low simulated S_{conf} is that for any point term distribution spanning a range on the order 0 to -1 eV, this energy scale would dominate over that of thermal fluctuations, $kT \approx 25$ meV. Sites with the highest binding energy (the most negative point terms) fill first, then sites of lower binding energy are filled in sequence as the chemical potential (or Fermi level) of the electrode is changed, with little driving force to fill sites at different energy. This means that any given chemical potential, a limited number of states would be energetically accesssible, resulting in a low S_{conf}. In contrast, the experimental result suggests limited point term heterogeneity, with many sites of similar energy that are energetically accessible through thermal fluctuations, and an S_{conf} approximating solid solution filling of the interlayer

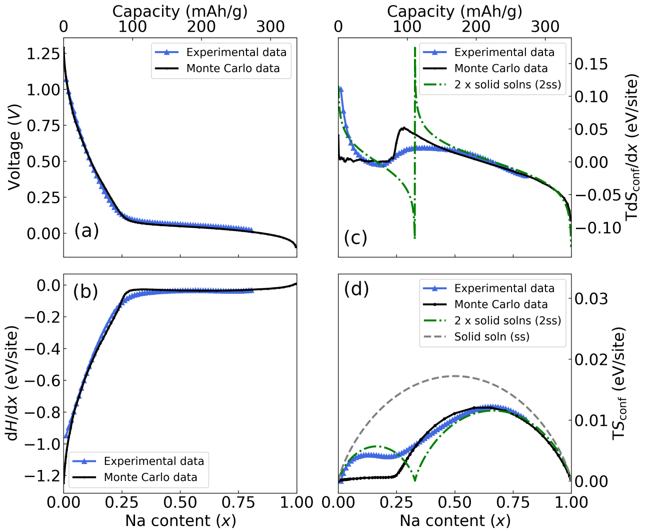

Figure 6: (a) Cell voltage, (b) partial molar (p.m.) enthalpy, (c) p.m. entropy, (d) configurational entropy. Black points: GCMC data, with a triangular distribution of interlayer point terms. Blue points: experimental data; grey dashed line: ideal solid solution (ss) on all sites; green dash-dot line: ideal ss filling of interlayer sublattice, followed by ss filling of nanopore sites.

sites. Therefore, *a priori* interlayer site heterogeneity, i.e. a distribution of point defect energies, is not the primary origin of the change in p.m. enthalpy, and therefore the change in voltage, in the sloping voltage region.

The same finding is also helpful to understand the possible role of Na adsorption on surface sites versus being inserted into the interlayers. This situation could also result in a distribution of point terms, because of different possible Na-C binding energies at the surface with respect to the bulk. By the same logic as above, the difference between the simulated and experimental configurational entropy suggests either that surface sites are a relatively small proportion of the available sites, the energetics of Na adsorption do not vary significantly from the bulk interlayer sites, or both. This justifies approximating the surface and interlayer sites as a single energy level in the model presented subsequently.

We consider that the interlayer point term, ϵ_1', might vary with sodiation fraction n_1. When an alkali metal is intercalated into a compound with a low density of states (DOS) at the Fermi level, large changes in chemical potential occur, as highlighted by Dahn et al. [37]. This results in rapid changes of the point term of lithium in graphite at low lithium occupation, resulting in additional electrochemical features [23]. Similarly, the local structure of hard carbons approximates to curved bilayer graphene, which also presents a low DOS at the Fermi level (Dirac cone at the Γ point minimum) when no sodium is in the lattice [38, 10]. In fact, Stratford et al. found localised charge transfer

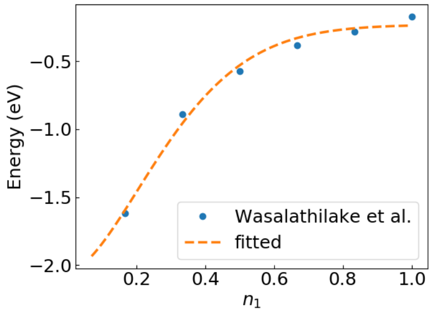

Figure 7: Blue points: DFT data obtained from Figure 6 of ref. [41], for sodium adsorption on graphene. Data re-used with permission from Elsevier Ltd., Copyright 2018. The binding energy as a function of sodium concentration, n_1 is obtained. The fitted function, obtained within the present work, is $E = A\exp(-\mathrm{Bn}_1^{1.67}) + \mathrm{y}_0$, where E is the adsorption energy of sodium on graphene. The fitting coefficients, obtained from least squares regression, were: $y_0 = -0.23$ eV, $A = -1.82$ eV, $B = 5.78$.

between sodium and carbon defects in hard carbons by in-situ NMR [10]. They found changes in the local environment of the sodium ions with an increase in the amount of sodium in the hard carbon, implying that the sodium species become increasingly metallic as the voltage decreases. A greater Knight shift was obtained with increasing sodium concentration, indicating an increase of the Na 2s DOS at the Fermi level. The operando Raman measurements of Euchner et al. combined with DFT calculations of phonon spectra, suggest a downwards shift in the G-band through as more sodium is added in the sloping region [38], which was also observed experimentally by Weaving et al. [13]. Both groups attributed this shift to charge transfer from the metal atoms to the carbon matrix [38, 13]. DFT calculations combined with Bader charge transfer analysis also suggest changes in the charge transfer from sodium to carbon dependent on the amount of inserted sodium [39, 40, 41].

Based on arguments presented previously for lithium in graphite [23, 37, 42] and the experimental/DFT evidence for the sodium in hard carbon system, it is therefore reasonable to assume that the interlayer point term, ϵ_1', varies dependent on the sodiation fraction, n_1. This is in line with the DFT data of Wasalathilake et al. [41], who showed a more negative binding energy, ΔE_{Na}, at low sodium occupation that decays to a less negative ΔE_{Na} as the lattice becomes sodiated. We show DFT data from Wasalthilake et al. in Figure 7, for sodium adsorption on graphene.

Consistently with these calculations, we found that a relationship of the form

$$\epsilon_1'(n_1) = \epsilon_1 + A\exp(-\mathrm{Bn}_1^{\mathrm{C}}), \tag{19}$$

gave a satisfactory fit to the experimental results for the partial molar enthalpy variation in the sloping region. Here ϵ_1 represents the interlayer point term in the limit of high sodium occupation, and A, B and C are empirical fitting constants that represent the amplitude, decay constant and exponent, respectively, of the point term variation with n_1, obtained from experimental data. Pairwise Na-Na interactions were tested, but were found to negligibly influence the thermodynamic behaviour compared with the variation in Na-C interactions expressed in equation 19. Therefore, pairwise interactions were neglected. As shown from the fitted variables in Table 2, $\epsilon_1'(n_1 = 0) = -1.056$ eV and $\epsilon_1'(n_1 = 1) = -0.477$ eV, i.e. there is a high sodium binding energy at low occupation, that decays to a somewhat lower binding energy once the lattice becomes filled. The quantitative values obtained for A and B by fitting the experimental thermodynamic profiles differ from those shown in Figure 7, which are based on DFT data [41]. Nevertheless, the experimental and DFT parameters are in qualitative agreement, with both parameter sets describing an exponentially decaying binding energy with the same sign and order of magnitude of the interaction. Quantitative differences between experiment and the model likely arise from the DFT exchange correlation functional, as well as planar graphene being an imperfect proxy system for hard carbon.

Results for the enthalpy variation of the interlayer and nanopore sites are presented in Figure 8. The presented results assume that sodium filling proceeds entirely in the interlayer sites (red line) until those are filled, and then further filling proceeds only in the nanopore sites. The enthalpy variation for $0 < x < 0.2$ is indeed described well under this assumption, but the p.m. entropy would be that of the green line shown in Figure 6. There is a transition region between about $0.2 < x < 0.5$, where filling of interlayer and nanopore sites is energetically competitive and proceeds at the same time, as shown schematically at three different sodiation degrees in Figure 9. This transition is naturally accounted for in the Bragg-Williams model, as outlined in the next section.

5.2 Bragg-Williams, Monte Carlo and experimental results compared

We can compare the results of the Bragg-Williams model, defined in section 4.1, with experiments. We utilise interlayer interaction term defined in equation 19, having provided physical arguments in the previous section. It is also possible to validate the Bragg-Williams results by putting the same interaction parameters into the grand canonical Hamiltonian (equation 18) and performing Monte Carlo calculations. Bragg-Williams, Monte Carlo and experimental thermodynamics results are thus overlaid in Figure 10.

It is apparent from all the plots in Figure 10 that the Monte Carlo and Bragg-Williams results, evaluated using the same interaction parameters but in two different ensembles, are in good agreement. This provides validation of the simulation results from both methods. The agreement between the results means that the substantially less computationally expensive Bragg-Williams results can be used to model the experimental behaviour.

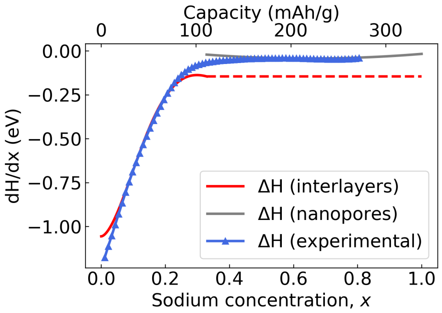

Figure 8: Red line: plot of the interlayer enthalpy variation obtained from equation 19, in the interval $0 < x < 0.329$, assuming that this region corresponds entirely to interlayer filling. The dashed red line is an extrapolation. Grey line: plot of the enthalpy variation in the nanopore filling region, obtained using the expression introduced in Table 2, also assuming that filling of these sites proceeds in the interval $0.329 < x < 1$. Blue line: experimental results.

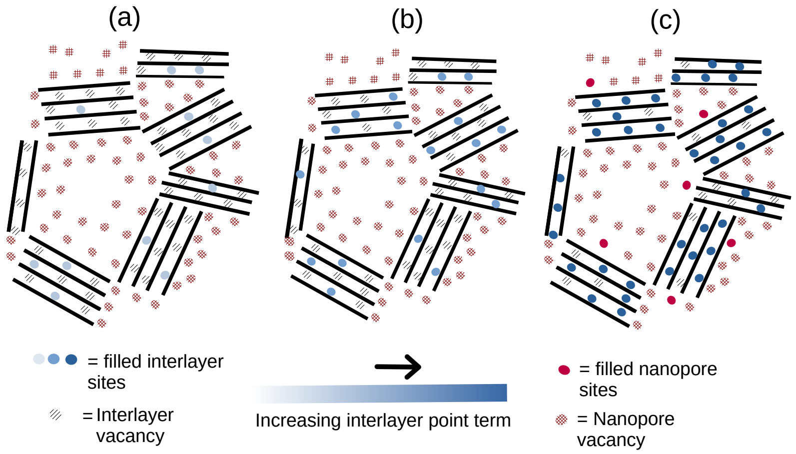

Figure 9: Schematic representation of the site occupancies and energies of sodium in hard carbon at three different sodiation fractions. As explained in the text, the energy of the interlayer sites varies with the number of occupied sites, as indicated by the changing shade of these sites. The point term of the nanopore sites, indicated in red, is fixed (although mean field interactions between Na particles are accounted for). As shown in (c), nanopore filling proceeds before all the interlayer sites are completely filled.

10.1002/cphc.202100748

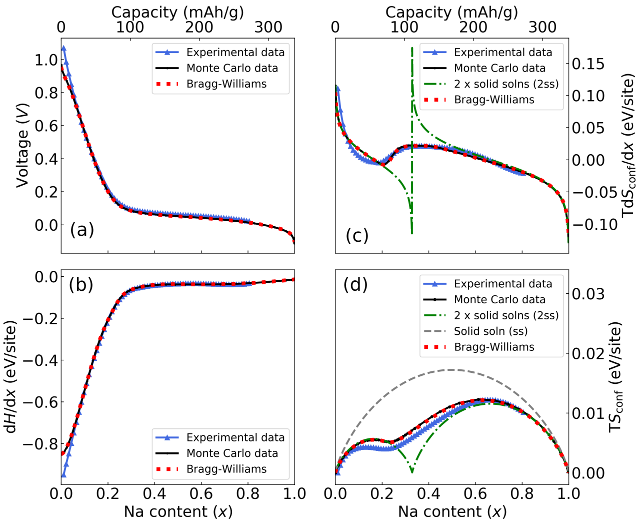

Figure 10: (a) Voltage, (b) partial molar (p.m.) enthalpy, (c) p.m. configurational entropy, (d) absolute configurational entropy. Bragg-Williams (red dashed line) and GCMC (black points) simulation results were obtained from equation 19, assuming an interlayer point term that varies with sodiation fraction. Blue points: experimental data; grey line: ideal solid solution (ss) on all sites (equation S7-S8); green dash-dot line: ideal ss filling of interlayer sublattice, followed by ss filling of nanopore sites (equation S12-S15).

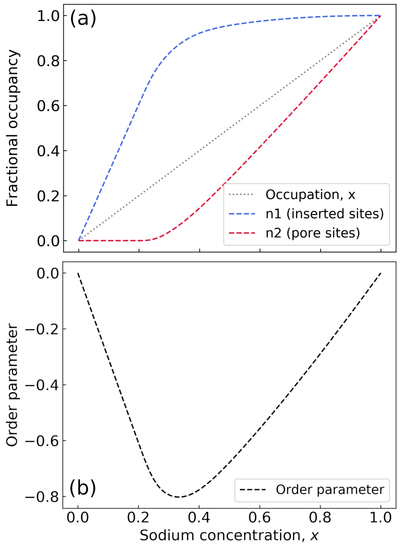

Figure 11: (a) Proportions of sodium occupying interlayer (n_1) and nanopore (n_2) sites as a function of sodiation fraction, x. (b) Order parameter (OP), obtained from equation S17.

Comparing those Bragg-Williams results to the experiments, good agreement is also obtained, indicating that both the energetics and the configurational entropy of sodiation in hard carbon are well described in the model. The three regions **1**: sloping region, **2**: transition and **3**: plateau region that were highlighted in Figure 2 in the experimental section are faithfully replicated.

A closer inspection of Figure 10d reveals that the experimental configurational entropy, $S_{\mathrm{conf}}(x)$, is somewhat lower than either than Bragg-Williams solution or the analytical solution for ideal solid solution filling of interlayers (green dash-dot line, determined from equation S12-S15). This could be due to a some small distribution of point terms in the interlayers (c.f. section 5.1) that is not captured within this model. A full treatment of this effect would require combining *a priori* heterogeneity with a varying interlayer point term with occupation. Alternatively, a more sophisticated model of the vibrational and/or electronic entropy may be required. Both of these aspects are beyond the scope of the present work. However, neglecting *a priori* heterogeneity is otherwise a very good approximation to the entropy of sodiation of hard carbon and allows all of the key parts of the voltage profile to be quantitatively decoupled.

The proportions of sodium occupying the carbon interlayers and the nanopores, n_1 and n_2, can be separated within the model, which is a key advantage of modelling the configurational entropy. This is shown in Figure 11a.

It is revealed that exclusive filling of the interlayers as an ideal solid solution proceeds first in region **1**, as previously hypothesised. Approximately 80% of the available interlayer capacity is filled in this region. However, in regions **2** and **3**, filling of nanopores proceeds at the same time as interlayer filling. In region **2**, significant filling of both regions occurs while in region **3**, filling of the nanopores predominates.

Additionally, we can quantify an order parameter (OP), defined in the Supplementary Information (equation S17). This OP is shown in Figure 11b as a function of x. The OP is negative for all x, indicating that a higher proportion of interlayer sites are filled than nanopore sites. Note that with $L < 0.5$ as in the results presented here, it is still possible for a greater *absolute* number of nanopore sites to be occupied even if the OP is negative, because there are more nanopore sites available to be filled. The minimum value of the OP at $x = 0.3$ is ≈ -0.8. Thus, nanopore filling initiates once about 80% of the available interlayer capacity is filled.

The energetic diffference between interlayer and nanopore sites means that only the interlayer sites, which comprise about one third of the total available capacity, can initially be filled. The restricted number of available configurations can be interpreted as ordering, which manifests itself as a local minimum in the entropy (Figure 10d). Commencement of nanopore filling, once the chemical potential of sodium comes close to that of bulk metallic sodium, is responsible for the increase in entropy once those configurations become energetically accessible. This behaviour is responsible the experimentally observed entropy features shown in Figure 10c-d.

5.3 Interpretation of nanopore interactions

In this section, we present further information about the nanopore interactions described by ϵ_2', defined earlier in equation 14.

The dQ/dV data presented in Figure 12, are sensitive to the interactions ϵ_2', since these interactions determine the slope of the voltage plateau. The peak position is primarily determined by $\epsilon_2 = -0.021$ eV. This ϵ_2 value, just slightly negative of 0 eV, can be interpreted as deposition of metallic sodium into the pores at potentials slightly *positive* of the equilibrium potential for reduction of sodium, i.e. underpotential deposition (UPD) [43, 44]. Note that UPD occurs because the interaction between the deposited metal atom and the substrate is more energetically favourable than metal-on-metal deposition, and thus UPD is restricted to one, or exceptionally two, monolayers.

The dQ/dV peak shape is determined by interactions between Na atoms in the pores. The experimental partial molar enthalpy, Figure 2a, showed two turning points in the nanopore filling region. This behaviour cannot be replicated with a single interparticle interaction term, which would cause a monotonic decrease or increase in ΔH dependent on whether that term is attractive or repulsive, respectively. However, two interaction terms $g_2 = -0.046$ eV and $g_3 = 0.032$ eV, was found to be sufficient to replicate the dQ/dV peak shape in Figure 12, and the p.m. enthalpy behaviour in Figure 2a. The term g_2 is analagous to a mean field pairwise interaction, while g_3 behaves like a triplet interaction, albeit a mean field one. As in previous sections, the agreement be-

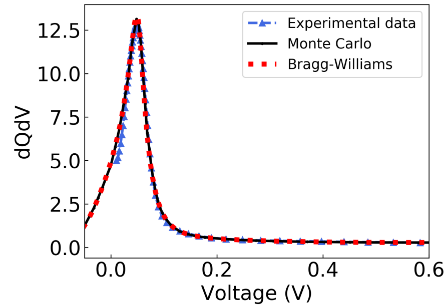

Figure 12: dQ/dV results. Blue points: experimental data; blue points: GCMC data; black points: red dashed line: Bragg-Williams (BW) solution.

tween the GCMC and Bragg-Williams (BW) results is strong, so we will discuss only the BW result. Both simulation methods replicate the experimental peak width and shape.

To gain additional insight into the interactions, we can separate the energetic contributions from the interlayers and nanopores from the BW model, since we know the fraction of these sites that are occupied at any given x value (Figure 11a). The full procedure is described in the Supplemental Information, section 2.4.

In Figure 13, the partial molar enthalpy of sodium in the interlayers and nanopores, $\Delta H_{\text{interlayers}}$ and $\Delta H_{\text{nanopores}}$ respectively, are shown. In contrast to the result shown earlier in Figure 8, this analysis accounts for the correct occupation of interlayer and nanopore sites at each x value. The enthalpy variation in the sloping region is dominated by interlayer interactions. Filling of nanopores commences at $x = 0.2$ and at $x = 0.4$, nanopore and interlayer filling become energetically competitive, resulting in a minimum in $-dH/dx$. At higher x, the energetic contributions from nanopore filling dominate. The second turning point in the partial molar enthalpy occurs just before $x = 1$ and originates from the nanopore interaction term. The simulated results replicate the two turning points found experimentally in the inset of Figure 2a. The first turning point originates from a transition from interlayer to nanopore filling. The second one appears to a consequence of two competitive interactions between Na atoms in the nanopores.

One hypothesis to explain the enthalpy relationship in the nanopores is the following, represented schematically in Figure 14. Deposition of sodium on the pore walls commences by a mechanism similar to UPD. It is likely that this is initiated on defect sites on the pore walls. As the cell voltage increases, the first layer completes (Figure 14a), as described by the ϵ_2 term. Ordinarily, subsequent sodium deposition (Figure 14b-c) should not be possible above 0 V vs. Na. However, we propose that pore geometry itself facilitates subsequent sodium deposition, because subsequent layers of sodium deposited onto the first

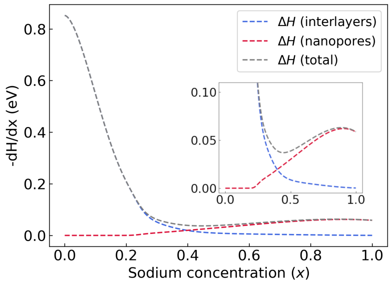

Figure 13: Plot of the partial molar enthalpy obtained from the Bragg-Williams model. The energetics of the interlayers (blue line) and nanopores (red line) were separated by applying equations S18-S20. The total partial molar enthalpy (grey line), presented earlier, is also shown here. Inset: the same data shown over a narrower energy range.

layer reduce the surface area and therefore the surface energy of the system. The g_2 term can be thought of a surface term; g_3 as a volume term. There is a competition between these terms, but interestingly this is the exact opposite of a nucleation and growth problem [45], because deposition reduces the surface energy of the system but increases the energy through the bulk term. This could be the reason that the system is well described by a negative g_2 but positive g_3, resulting in a maximum in $-dH/dx$.

Although we have no evidence of this hypothesis other than measurement and modelling of the energy terms and the trend with sodiation fraction, we believe this should be examined further on systematically synthesised hard carbons of variable pore size and geometry, perhaps bolstered by *operando* techniques such as small angle x-ray scattering (SAXS). Youn et al. recently found, via DFT calculations, that layers of sodium of between 3-6 atomic layers in thickness are stable in between two sheets of planar graphene [46]. With a nearest neighbour distance in body-centred cubic sodium of 0.366 nm [47], this regime spans a pore diameter range between about 1.1 and 2.2 nm. Consistent with this size range, a pore size of approximately 2.0 nm was obtained by Au et al. using SAXS for hard carbons showing the highest capacity of about 300 mAh/g [11], indicating that the energetics of multiple layer sodium adsorption in nanopores is worth further study.

6 Conclusions

In this work, we present the first application of the entropy profiling technique, which is an established method for characterising lithium-ion cells, to any sodium-ion system. It was demonstrated that this method, when applied to sodiation of hard carbon, yields additional features that ordinarily cannot be discerned through conventional galvanostatic cycling. The method was sucess-

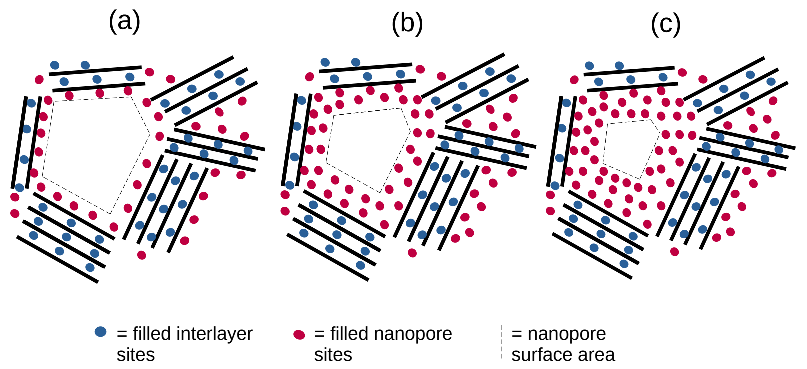

Figure 14: Schematic representation of how the nanopore site distribution might change with increasing sodiation fraction from (a) to (c). The dashed grey line represents the surface area of the empty void. As the sodiation fraction increases, the surface area of that void decreases.

fully combined with lattice gas models that allows the interlayer and nanopore site environments to be separated. We can break down the main findings as follows:

- The energetics and entropy of sodium insertion in hard carbon were determined experimentally.
- The observed entropy profile feature was attributed to: **1**: a region where only interlayer sites were filled at low sodium occupation, **2**: a region where interlayer and nanopore sites were filled at the same time and **3**: a region corresponding almost entirely to nanopore filling, with the interlayer sites almost all filled. Regions **1**, **2** and **3** correspond to the observed decrease, increase and decrease in partial molar entropy, respectively, with additional sodium occupation.
- We developed a 2 level Bragg-Williams model, the first level corresponding to sodiation of the carbon interlayers and the second to sodiation of the nanopores. The method was validated by fitting the interaction terms to the experimental thermodynamic results. The calculation of the partition function was validated through Monte Carlo simulations, which yielded nearly identical results to the Bragg-Williams model.
- To simultaneously model the energetics and entropy of sodium insertion into the interlayers, it was necessary to account for changes in the interaction between sodium and the carbon host with the interlayer filling fraction, which can be attributed to varying charge transfer between sodium

and the host dependent on sodiation fraction, i.e. the system becomes more metallic as more sodium is inserted.

- Modelling the enthalpy changes in the interlayers with a distribution of point terms, which would arise from defects in the interlayers, leads to a description of the entropy that is inconsistent with experimental results.
- Quantification of the interlayer and nanopore sublattices suggests that, for the studied hard carbon sample, the sloping region corresponds to filling of only the interlayer sites to about 80% of their available capacity. The plateau region is attributed to filling of the remaining interlayer sites with concomittant filling of nanopores.
- Fitting the model to experiment required extrapolating the curves beyond the experimental maximum capacity. The theoretical capacity was 338 mAh/g while the experimental discharge capacity was approximately 270 mAh/g. Almost all of the unutilised capacity was in the nanopores.

As outlook from the work, we anticipate that entropy profiling could become a standard method for the characterisation of hard carbon materials of controlled pore size and interlayer geometry. It has the potential to allow more definitive discrimination between the plateau and sloping voltage regions dependent on synthesis conditions. Hard carbon materials design strategies should focus, not only on optimising the capacity in these regions, but also on raising the voltage of the plateau region. This could be achieved through systematic doping, such as through boron substitution, which should allow additional capacity to be accessed in the nanopores. As an additional benefit, such a strategy would mitigate the risk of sodium plating.

7 Acknowledgments

M.P. Mercer, A.A. Zülke and H.E. Hoster thank the Faraday Institution (faraday.ac.uk; EP/S003053/1), grant number FIRG025, for funding. This work contributes to the research performed at CELEST (Center for Electrochemical Energy Storage Ulm-Karlsruhe) and was funded by the German Research Foundation (DFG) under Project ID 390874152 (POLiS Cluster of Excellence). E.P.M. Leiva acknowledges grants PIP CONICET 11220200101189CO, PUE/2017 CONICET, FONCYT PICT-2015-1605. M.P. Mercer and S. Affleck acknowledge support of the High End Computing facility at Lancaster University. M.P. Mercer also thanks Dr. Jamie Fairbrother from the Department of Management Science at Lancaster University for feedback on the numerical optimisation procedure and for coding advice to speed up the partition function calculation.

References

[1] J.-M. Tarascon and M. Armand. Issues and challenges facing rechargeable lithium batteries. *Nature*, 414:359–367, 2001.

[2] Holger C. Hesse, Michael Schimpe, Daniel Kucevic, and Andreas Jossen. Lithium-ion battery storage for the grid—a review of stationary battery storage system design tailored for applications in modern power grids. *Energies*, 10:2107, 2017.

[3] Environmental impacts of lithium metal polymer and lithium-ion stationary batteries. *Renew. Sust. Energ. Rev.*

[4] Nuria Tapia-Ruiz, A Robert Armstrong, Hande Alptekin, Marco A Amores, Heather Au, Jerry Barker, Rebecca Boston, William R Brant, Jake M Brittain, Yue Chen, Manish Chhowalla, Yong-Seok Choi, Sara I R Costa, Maria Crespo Ribadeneyra, Serena A Cussen, Edmund J Cussen, William I F David, Aamod V Desai, Stewart A M Dickson, Emmanuel I Eweka, Juan D Forero-Saboya, Clare P Grey, John M Griffin, Peter Gross, Xiao Hua, John T S Irvine, Patrik Johansson, Martin O Jones, Martin Karlsmo, Emma Kendrick, Eunjeong Kim, Oleg V Kolosov, Zhuangnan Li, Stijn F L Mertens, Ronnie Mogensen, Laure Monconduit, Russell E Morris, Andrew J Naylor, Shahin Nikman, Christopher A O'Keefe, Darren M C Ould, R G Palgrave, Philippe Poizot, Alexandre Ponrouch, Stéven Renault, Emily M Reynolds, Ashish Rudola, Ruth Sayers, David O Scanlon, S Sen, Valerie R Seymour, Begoña Silván, Moulay Tahar Sougrati, Lorenzo Stievano, Grant S Stone, Chris I Thomas, Maria-Magdalena Titirici, Jincheng Tong, Thomas J Wood, Dominic S Wright, and Reza Younesi. 2021 roadmap for sodium-ion batteries. *J. Phys. Energy*, 3:031503, 2021.

[5] Fei Xie, Zhen Xu, Zhenyu Guo, and Maria-Magdalena Titirici. Hard carbons for sodium-ion batteries and beyond. *Prog. Energy*, 2:042002, 2020.

[6] A. Metrot, D. Guerard, D. Billaud, and A. Herold. New results about the sodium-graphite system. *Synth. Met.*, 1:363–369, 1980.

[7] D. A. Stevens and J. R. Dahn. High capacity anode materials for rechargeable sodium-ion batteries. *J. Electrochem. Soc.*, 147:1271, 2000.

[8] D. A. Stevens and J. R. Dahn. The mechanisms of lithium and sodium insertion in carbon materials. *J. Electrochem. Soc.*, 148:A803, 2001.

[9] Joshua M. Stratford, Annette K. Kleppe, Dean S. Keeble, Philip A. Chater, Seyyed Shayan Meysami, Christopher J. Wright, Jerry Barker, Maria-Magdalena Titirici, Phoebe K. Allan, and Clare P. Grey. Correlating local structure and sodium storage in hard carbon anodes: Insights from pair distribution function analysis and solid-state nmr. *J. Am. Chem. Soc.*, 143:14274–14286, 2021.

[10] Joshua M. Stratford, Phoebe K. Allan, Oliver Pecher, Philip A. Chater, and Clare P. Grey. Mechanistic insights into sodium storage in hard carbon anodes using local structure probes. *Chem. Commun.*, 52:12430–12433, 2016.

[11] Heather Au, Hande Alptekin, Anders C. S. Jensen, Emilia Olsson, Christopher A. O'Keefe, Thomas Smith, Maria Crespo-Ribadeneyra, Thomas F. Headen, Clare P. Grey, Qiong Cai, Alan J. Drew, and Maria-Magdalena Titirici. A revised mechanistic model for sodium insertion in hard carbons. *Energy Environ. Sci.*, 13:3469–3479, 2020.

[12] M. Anji Reddy, M. Helen, Axel Groß, Maximilian Fichtner, and Holger Euchner. Insight into sodium insertion and the storage mechanism in hard carbon. *ACS Energy Lett.*, 3:2851–2857, 2018.

[13] Julia S. Weaving, Alvin Lim, Jason Millichamp, Tobias P. Neville, Daniela Ledwoch, Emma Kendrick, Paul F. McMillan, Paul R. Shearing, Christopher A. Howard, and Dan J.L. Brett. Elucidating the sodiation mechanism in hard carbon by operando raman spectroscopy. *ACS Appl. Energy Mater.*, 3:7474–7484, 2020.

[14] Kei Kubota, Saori Shimadzu, Naoaki Yabuuchi, Satoshi Tominaka, Soshi Shiraishi, Maria Abreu-Sepulveda, Ayyakkannu Manivannan, Kazuma Gotoh, Mika Fukunishi, Mouad Dahbi, and Shinichi Komaba. Structural analysis of sucrose-derived hard carbon and correlation with the electrochemical properties for lithium, sodium, and potassium insertion. *Chem. Mater.*, 32:2961–2977, 2020.

[15] Dequan Chen, Wen Zhang, Kangying Luo, Yang Song, Yanjun Zhong, Yuxia Liu, Gongke Wang, Benhe Zhong, Zhenguo Wu, and Xiaodong Guo. Hard carbon for sodium storage: mechanism and optimization strategies toward commercialization. *Energy Environ. Sci.*, 14:2244–2262, 2021.

[16] M.Z.A. Munshi and W.H. Smyrl. Insertion reactions of sodium in v6o13 single crystals from a solid polymeric electrolyte. *Solid State Ion.*, 45:183–189, 1991.

[17] E. Markevich, M.D. Levi, and D. Aurbach. Comparison between potentiostatic and galvanostatic intermittent titration techniques for determination of chemical diffusion coefficients in ion-insertion electrodes. *J. Electroanal. Chem.*, 580:231–237, 2005.

[18] Zhuo-Er Yu, Yingchun Lyu, Yeting Wang, Shuyin Xu, Hongyu Cheng, Xiaoyang Mu, Jiaqi Chu, Riming Chen, Yang Liu, and Bingkun Guo. Hard carbon micro-nano tubes derived from kapok fiber as anode materials for sodium-ion batteries and the sodium-ion storage mechanism. *Chem. Commun.*, 56:778–781, 2020.

[19] Yong Huang, Yuqing Wang, Panxing Bai, and Yunhua Xu. Storage mechanism of alkali metal ions in the hard carbon anode: an electrochemical viewpoint. *ACS Appl. Mater. Interfaces*, 13:38441–38449, 2021.

[20] Michael P. Mercer, Sophie Finnigan, Denis Kramer, Daniel Richards, and Harry E. Hoster. The influence of point defects on the entropy profiles of

lithium ion battery cathodes: a lattice-gas monte carlo study. *Electrochim. Acta*, 241:141 – 152, 2017.

[21] Steffen Schlueter, Ronny Genieser, Daniel Richards, Harry E. Hoster, and Michael P. Mercer. Quantifying structure dependent responses in li-ion cells with excess li spinel cathodes: matching voltage and entropy profiles through mean field models. *Phys. Chem. Chem. Phys.*, 20:21417–21429, 2018.

[22] Michael Peter Mercer, Chao Peng, Cindy Soares, Harry Ernst Hoster, and Denis Kramer. Voltage hysteresis during lithiation/delithiation of graphite associated with meta-stable carbon stackings. *J. Mater. Chem. A*, 9:492–504, 2021.

[23] Michael P. Mercer, Manuel Otero, Miriam Ferrer-Huerta, Agustin Sigal, Daniel E. Barraco, Harry E. Hoster, and Ezequiel P.M. Leiva. Transitions of lithium occupation in graphite: A physically informed model in the dilute lithium occupation limit supported by electrochemical and thermodynamic measurements. *Electrochim. Acta*, 324:134774, 2019.

[24] Patrick J. Osswald, Manuel del Rosario, Jürgen Garche, Andreas Jossen, and Harry E. Hoster. Fast and accurate measurement of entropy profiles of commercial lithium-ion cells. *Electrochim. Acta*, 177:270–276, 2015.

[25] Yvan Reynier, Jason Graetz, Tabitha Swan-Wood, Peter Rez, Rachid Yazami, and Brent Fultz. Entropy of Li intercalation in $li_x coo_2$. *Phys. Rev. B*, 70:174304, 2004.

[26] Y Reynier, R Yazami, and B Fultz. The entropy and enthalpy of lithium intercalation into graphite. *J. Power Sources*, 119-121:850 – 855, 2003.

[27] Xiao-Feng Zhang, Yan Zhao, Yatish Patel, Teng Zhang, Wei-Ming Liu, Mu Chen, Gregory J. Offer, and Yue Yan. Potentiometric measurement of entropy change for lithium batteries. *Phys. Chem. Chem. Phys.*, 19:9833–9842, 2017.

[28] David Allart, Maxime Montaru, and Hamid Gualous. Model of Lithium Intercalation into Graphite by Potentiometric Analysis with Equilibrium and Entropy Change Curves of Graphite Electrode. *J. Electrochem. Soc.*, 165:A380–A387, 2018.

[29] Rachid Yazami and Yvan Reynier. Thermodynamics and crystal structure anomalies in lithium-intercalated graphite. *J. Power Sources*, 153:312 – 318, 2006.

[30] Karen E. Thomas and John Newman. Heats of mixing and of entropy in porous insertion electrodes. *J. Power Sources*, 119-121:844 – 849, 2003.

[31] M.D Levi and D Aurbach. Frumkin intercalation isotherm — a tool for the description of lithium insertion into host materials: a review. *Electrochim. Acta*, 45:167–185, 1999.

[32] E. P. M. Leiva, E. Perassi, and D. Barraco. Shedding light on the entropy change found for the transition stage II→stage I of li-ion storage in graphite. *J. Electrochem. Soc.*, 164(1):A6154–A6157, 2016.

[33] Nicholas Metropolis, Arianna W. Rosenbluth, Marshall N. Rosenbluth, Augusta H. Teller, and Edward Teller. Equation of state calculations by fast computing machines. *J. Chem. Phys.*, 21:1087–1092, 1953.

[34] E. M. Gavilán-Arriazu, O. A. Pinto, B. A. López de Mishima, E. P. M. Leiva, and O. A. Oviedo. Grand canonical monte carlo study of li intercalation into graphite. *J. Electrochem. Soc.*, 165:A2019–A2025, 2018.

[35] Biwei Xiao, Teófilo Rojo, and Xiaolin Li. Hard carbon as sodium-ion battery anodes: Progress and challenges. *ChemSusChem*, 12:133–144, 2019.

[36] Ning Sun, Huan Liu, and Bin Xu. Facile synthesis of high performance hard carbon anode materials for sodium ion batteries. *J. Mater. Chem. A*, 3:20560–20566, 2015.

[37] J. R. Dahn, J. N. Reimers, A. K. Sleigh, and T. Tiedje. Density of states in graphite from electrochemical measurements on $\mathrm{li}_x(\mathrm{c}_{1-z}\mathrm{b}_z)_6$. *Phys. Rev. B*, 45:3773–3777, 1992.

[38] Holger Euchner, Bhaghavathi P. Vinayan, M. Anji Reddy, Maximilian Fichtner, and Axel Groß. Alkali metal insertion into hard carbon – the full picture. *J. Mater. Chem. A*, 8:14205–14213, 2020.

[39] Zhaohua Wang, Xin Feng, Ying Bai, Haoyi Yang, Ruiqi Dong, Xinran Wang, Huajie Xu, Qiyu Wang, Hong Li, Hongcai Gao, and Chuan Wu. Probing the Energy Storage Mechanism of Quasi-Metallic Na in Hard Carbon for Sodium-Ion Batteries. *Adv. Energy Mater.*, 11:2003854, 2021.

[40] Clement Bommier, Xiulei Ji, and P. Alex Greaney. Electrochemical properties and theoretical capacity for sodium storage in hard carbon: Insights from first principles calculations. *Chem. Mater.*, 31:658–677, 2019.

[41] Kimal Chandula Wasalathilake, Godwin A. Ayoko, and Cheng Yan. Effects of heteroatom doping on the performance of graphene in sodium-ion batteries: A density functional theory investigation. *Carbon*, 140:276–285, 2018.

[42] E. M. Gavilán-Arriazu, J. M. Hümöller, O. A. Pinto, B. A. López de Mishima, E. P. M. Leiva, and O. A. Oviedo. Fractional and integer stages of lithium ion–graphite systems: the role of electrostatic and elastic contributions. *Phys. Chem. Chem. Phys.*, 22:16174–16183, 2020.

[43] Enrique Herrero, Lisa J. Buller, and Héctor D. Abruña. Underpotential deposition at single crystal surfaces of au, pt, ag and other materials. *Chem. Rev.*, 101:1897–1930, 2001.

[44] D.M. Kolb, M. Przasnyski, and H. Gerischer. Underpotential deposition of metals and work function differences. *J. Electroanal. Chem.*, 54(1):25–38, 1974.

[45] E. Budevski, G. Staikov, and W.J. Lorenz. Electrocrystallization: Nucleation and growth phenomena. *Electrochim. Acta*, 45(15):2559–2574, 2000.

[46] Yong Youn, Bo Gao, Azusa Kamiyama, Kei Kubota, Shinichi Komaba, and Yoshitaka Tateyama. Nanometer-size na cluster formation in micropore of hard carbon as origin of higher-capacity na-ion battery. *npj Computational Materials*, 7:48, 2021.

[47] W. Adlhart, G. Fritsch, A. Heidemann, and E. Luescher. Measurement of the lattice parameter of sodium by neutron-back-scattering. *Phys. Lett. A*, 47:91–92, 1974.